

**Lifetime measurements in the tungsten isotopes  $^{176,178,180}\text{W}$** A. Harter,<sup>1,\*</sup> L. Knafla,<sup>1</sup> G. Friebner,<sup>1</sup> G. Häfner,<sup>1,2</sup> J. Jolie,<sup>1</sup> A. Blazhev,<sup>1</sup> A. Dewald,<sup>1</sup> F. Dunkel,<sup>1</sup> A. Esmaylzadeh,<sup>1</sup> C. Fransen,<sup>1</sup> V. Karayonchev,<sup>1</sup> K. Lawless,<sup>1</sup> M. Ley,<sup>1</sup> J.-M. Régis,<sup>1</sup> and K. O. Zell<sup>1</sup><sup>1</sup>Universität zu Köln, Mathematisch-Naturwissenschaftliche Fakultät, Institut für Kernphysik, 50937 Köln, Germany<sup>2</sup>Université Paris-Saclay, CNRS/IN2P3, IJCLab, F-91405 Orsay, France

(Received 27 October 2021; revised 7 June 2022; accepted 10 August 2022; published 24 August 2022)

Lifetimes of yrast states in the rare-earth midshell isotopes  $^{176,178,180}\text{W}$  have been measured with fast-timing methods using the Cologne iron-free Orange spectrometer and the Cologne HORUS spectrometer and with the recoil distance Doppler shift method using the Cologne coincidence plunger setup. Different fusion evaporation reactions have been used to populate excited states in the investigated nuclei. Lifetimes of the  $2_1^+$ ,  $4_1^+$ ,  $6_1^+$ , and  $8_1^+$  yrast states were measured in all three tungsten isotopes and in addition the lifetime of the  $10_1^+$  state was measured in  $^{176}\text{W}$ . Quadrupole deformation parameters, reduced transition probabilities, and  $B_{4/2}$  ratios are extracted and discussed in the context of interacting boson model 1 calculations. The results with newly determined signatures largely confirm the investigated tungsten isotopes to be deformed prolate rotors.

DOI: [10.1103/PhysRevC.106.024326](https://doi.org/10.1103/PhysRevC.106.024326)**I. INTRODUCTION**

The rare-earth midshell mass region around  $A = 178$  is characterized by a rich abundance of transitional nuclear structure phenomena [1–3]. This is caused by a competition between the microscopic nature of underlying single-particle structures and collective shape degrees of freedom [4]. The former dominates towards the proton shell closure ( $Z = 82$ ) and the latter is particularly pronounced with increasing valence nucleons or holes. The tungsten isotopes ( $Z = 74$ ) around the neutron midshell ( $N = 104$ ) lie at the edge of the strongly collective quadrupole deformed mass region around  $^{170}\text{Dy}$  [5]. Therefore, the measurement of the collective signatures of the even-even tungsten isotopes around the neutron midshell makes a decisive contribution to the delimitation of this transition region itself.

It was suggested that the investigated nuclei lie close to the X(5) critical point symmetry region [6] with a shape phase transition from spherical shapes to axially symmetric prolate shapes around  $^{178}\text{Os}$  [7–9]. This assumption could not be confirmed due to the unclear or incomplete data situation [9]. Moreover, nuclear collectivity and shape transition in rotorlike regions are usually described in terms of, e.g., the excitation energy of the first excited  $2_1^+$  state as well as its ratio to the first excited  $4_1^+$  state, called  $R_{4/2}$ , or the transition strength of the  $2_1^+ \rightarrow 0_1^+$  ground state transition and its ratio to the transition strength of the  $4_1^+ \rightarrow 2_1^+$  transition, called  $B_{4/2}$  [10]. The  $B_{4/2}$  ratio is an indication for the  $\gamma$  softness of the potential [11–13] and can also be used as a signature for shape phase transitions [6,14]. For deformed nuclei the ratio can show deviations from the Alaga rule value of  $10/7$ . Therefore, the measurement of the tungsten isotopes  $^{176,178,180}\text{W}$ , with regard

to the transition strengths of the low-spin yrast states, forms an interesting contribution to the understanding of the nuclear structure transitions in this region.

The low excitation energies of the  $2_1^+$  states, as well as the  $R_{4/2}$  ratios, show a clear tendency towards axially symmetric rotor properties [10,15–17]. Therefore, the question arises whether this tendency is confirmed by the evolution of the  $B_{4/2}$  ratio and pronounced transition strengths of the low-spin yrast states. Consequently, the characterization of the midshell surrounding tungsten isotopes with special regard to the transition strengths of the low-spin yrast states and the  $B_{4/2}$  ratios is an interesting prospect, especially since the data are incomplete [18]. In particular, for  $^{176,180}\text{W}$  the  $B_{4/2}$  ratio is unknown. The  $B(E2; 2_1^+ \rightarrow 0_1^+)$  values are already known for all isotopes. For  $^{178}\text{W}$ , the  $B(E2; 4_1^+ \rightarrow 2_1^+)$  and an upper limit for the  $B(E2; 6_1^+ \rightarrow 4_1^+)$  were published recently [19].  $B(E2; I \rightarrow I - 2)$  values of higher-lying yrast states are completely unknown so far.

To fill these gaps, lifetime measurements of yrast states were carried out for the isotopes  $^{176,178,180}\text{W}$ . The new lifetimes allow to obtain  $B(E2)$  values for the low-spin yrast states of the given nuclei. Lifetimes of the low-spin yrast states in the investigated tungsten isotopes were measured using fast-timing methods. Additionally, lifetimes of the  $6_1^+$ ,  $8_1^+$ , and  $10_1^+$  states in  $^{176}\text{W}$  were measured with the Cologne coincidence plunger using the differential decay curve method (DDCM) [20]. The fast-timing experiments for the lifetime measurement of  $^{178,180}\text{W}$  were performed using the Cologne iron-free Orange conversion electron spectrometer. The experiment for  $^{176}\text{W}$  was performed using the Cologne HORUS cube spectrometer, equipped with  $\text{LaBr}_3(\text{Ce})$  fast-timing scintillators (LaBr) and high-resolution high-purity germanium (HPGe) detectors. Not all nuclides were measured by the plunger method because this method requires high recoil velocities of the reaction product nuclei to allow the necessary

\*Corresponding author: [aharter@ikp.uni-koeln.de](mailto:aharter@ikp.uni-koeln.de)

Doppler shifts of the  $\gamma$  lines. These were sufficiently given only in the reaction for  $^{176}\text{W}$ , and even that only at  $\gamma$  energies above 300 keV.

The excitation energies of the  $2_1^+$  states lie barely higher than 100 keV. Hence, the  $\gamma$ -ray emission is highly dominated by the internal conversion process and the emission of conversion electrons (ce) [21]. A suitable instrument to measure conversion electrons is an iron-free Orange spectrometer [22]. An Orange spectrometer consists of specially shaped copper coils to induce a magnetic field through a circulating current. Based on the applied current, electrons with a specific momentum can be selected and deflected into the narrow detector entrance window [23]. The high selectivity of the Orange spectrometer allows for a precise electron gate, specifying the cascade of interest. This allows for accurate  $e^-$ - $\gamma$  and electron tagged  $\gamma$ - $\gamma$  fast timing ( $e^-$ - $\gamma$ - $\gamma$ ) to access lifetimes in the subnanosecond regime [18,24].

The experimental details with a special emphasis on the Orange spectrometer in combination with  $\text{LaBr}_3(\text{Ce})$  fast-timing scintillators for  $e^-$ - $\gamma$ - $\gamma$  and  $e^-$ - $\gamma$  fast timing as well as the recoil distance Doppler-shift method are summarized in Sec. II. The experimental results are presented in Sec. III. The analysis of the data and the presentation of the results are followed by theoretical calculations in the framework of the interacting boson model [25] in order to be able to classify the results in a well-known context. Here, the interacting boson model 1 (IBM-1), where no distinction between protons and neutrons is made, was chosen as a successful model in collective regions [10].

## II. EXPERIMENTAL DETAILS

All experiments were conducted at the 10 MV FN Tandem accelerator of the Institut für Kernphysik (IKP) in Cologne. Excited states in  $^{176,178,180}\text{W}$  were populated via different fusion-evaporation reactions:  $^{164}\text{Dy}(^{16}\text{O}, 4n)^{176}\text{W}$  at beam energy of 80 MeV,  $^{172}\text{Yb}(^9\text{Be}, 3n)^{178}\text{W}$  at beam energy of 40 MeV, and  $^{181}\text{Ta}(^1\text{H}, 2n)^{180}\text{W}$  at beam energy of 16 MeV.

For the populating reactions the self-supporting targets  $^{164}\text{Dy}$ , 7 mg/cm<sup>2</sup> (in HORUS) and 0.9 mg/cm<sup>2</sup> (in plunger),  $^{172}\text{Yb}$ , 1 mg/cm<sup>2</sup>, and  $^{181}\text{Ta}$ , 0.5 mg/cm<sup>2</sup>, were used. The lifetimes were measured using the fast-timing technique in combination with the generalized centroid difference (GCD) method [26] as well as the recoil distance Doppler-shift (RDDS) method [27]. The reaction  $^{164}\text{Dy}(^{16}\text{O}, 4n)^{176}\text{W}$  was used both for the fast-timing experiment at the HORUS spectrometer and for the RDDS measurement at the Cologne coincidence plunger setup. The  $^{172}\text{Yb}(^9\text{Be}, 3n)^{178}\text{W}$  and  $^{181}\text{Ta}(^1\text{H}, 2n)^{180}\text{W}$  experiments were performed at the Cologne Orange spectrometer setup.

### A. Experiments with the IKP iron-free Orange spectrometer

The experiments to measure lifetimes in  $^{178,180}\text{W}$  were performed at the Orange spectrometer [22] of the IKP using  $e^-$ - $\gamma$  and  $e^-$ - $\gamma$ - $\gamma$  timing with  $\text{LaBr}_3(\text{Ce})$  scintillators. Lifetimes of the  $2_1^+$ ,  $4_1^+$ , and  $6_1^+$  states and an upper limit for the lifetime of the  $8_1^+$  state were determined for both isotopes. The conversion electron spectroscopy using the iron-free Or-

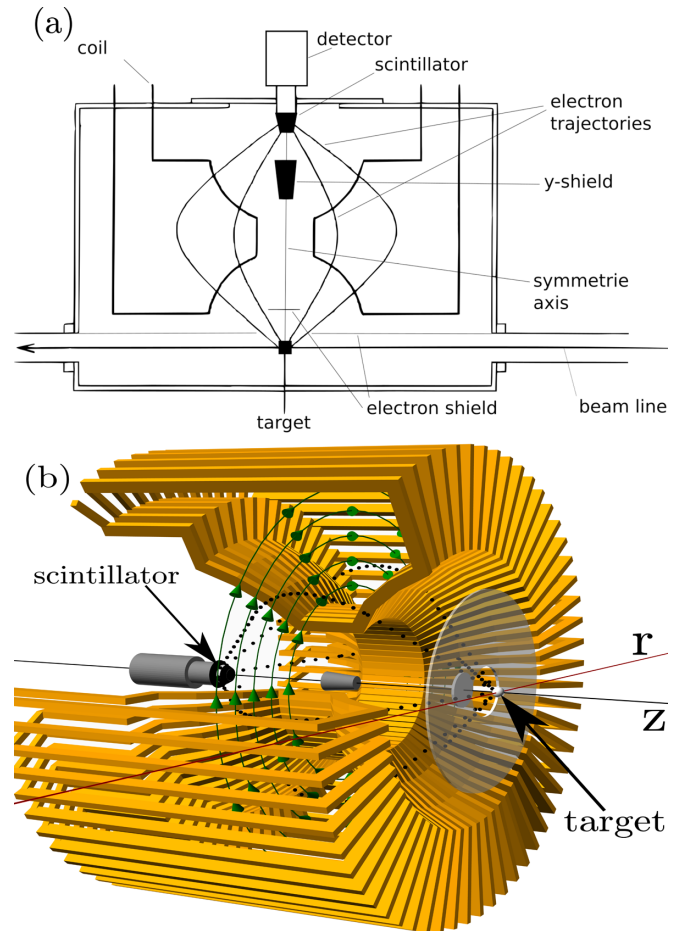


FIG. 1. (a) The elements of the Orange spectrometer, shown in a section through an  $(r, z)$  plane [30]. (b) Schematic three-dimensional model of the Orange spectrometer. The copper coils are drawn in orange. The magnetic field is indicated by the green circular arrows inside the coil volume. The circular electron shields are shown by the transparent light gray forms. The dark gray cone represents the  $\gamma$ -ray shield to shield the electron detector from unwanted  $\gamma$  rays. Possible flight trajectories of detected electrons are displayed by the black dotted curves. The symmetry axis ( $z$ ) is displayed in black and the beam axis ( $r$ ) in red.

ange spectrometer is a well-established method at the IKP [22,24,28,29]. The operating hardware as well as the controlling software was revised in 2018–2019 and, consequently, the two experiments performed in this work were also used as a commissioning of the new system.

The basic idea of an Orange spectrometer is the deflection of charged particles (i.e., conversion electrons) by a toroidal magnetic field generated by a current  $I$  circulating through specially shaped copper coils (see Fig. 1) yielding [23,31]

$$B = \mu_0 \frac{NI}{2\pi r}. \quad (1)$$

Here,  $\mu_0$  is the magnetic permeability,  $r$  the distance to the axis of symmetry, and  $N$  the number of windings. A schematic sketch of the system is presented in Fig. 1(a). The electrons are emitted from the target in a straight line towards the Orange coils and are deflected in the magnetic field towards

a plastic scintillation counter of type NE102 [22]. Based on the assumption that the electron source (target) is pointlike, it is assumed that the electrons with a selected momentum that enter the magnetic field move in the  $(r, z)$  plane of a winding, as displayed in Fig. 1(a). Electrons that do not fulfill the momentum condition do not reach the detector. An electron with velocity  $v$  is forced on a cycloid trajectory with rotation radius  $\rho_B$  which can be obtained from the radius of curvature  $\rho$  for homogeneous magnetic fields [31]:

$$m \frac{v^2}{\rho} = evB. \quad (2)$$

$B$  is calculated according to Eq. (1) and  $m = \frac{m_0}{\sqrt{1-(\frac{v}{c})^2}}$  is the relativistic mass of an electron. It follows that [23]

$$eB\rho = p = \frac{\rho \mu_0 N}{r 2\pi} I, \quad (3)$$

where  $\rho/r$  is a constant of the specific spectrometer depending on the shape of the coils. The electron momentum  $p$  can be expressed by the rigidity  $B\rho$  due to the proportionality of the electron momentum and the magnetic field strength or the coil current. By varying the coil current and the magnetic field, respectively, the energy of the electrons to be deflected into the plastic scintillator can be selected. By substituting Eq. (3) into the total relativistic energy

$$E_{\text{tot}} = \sqrt{(m_0 c^2)^2 + p^2 c^2} = E_e + m_0 c^2,$$

one obtains the relationship between the electron energy and the magnetic rigidity  $B\rho$ :

$$E_e = \sqrt{(m_0 c^2)^2 + e^2 c^2 (B\rho)^2} - m_0 c^2. \quad (4)$$

The energy spectra of the scintillator counter of the Orange spectrometer are usually contaminated by an exponentially decreasing  $\delta$ -electron background, which is unavoidable in in-beam ion reaction experiments [32], as displayed in Fig. 2. The energy transfer through inelastic Coulomb scattering is sufficient to ionize the colliding target atoms and projectile ions. Thus, excited electrons are emitted as  $\delta$  electrons in a cone opening in the beam direction. The  $\delta$ -electron background increases with the target thickness and the energy and charge number of the projectile.

Electron shields consisting of aluminum are attached to the inside of the spectrometer, blocking the straight path between the target and the scintillator. The Orange spectrometer at the IKP Cologne has a spatial opening angle of  $50^\circ$  [22]. This corresponds to a solid angle coverage of approximately 15–20 % of  $4\pi$  depending on the opening width of the ring slot of the scintillator counter. In combination with the efficiency of larger than 95% of the plastic scintillator for electrons with energies more than 15 keV, this leads to an electron detection efficiency of up to 20%.

In the present experiments, electron events were used as timing signals for  $e^- \gamma$  timing and as trigger signal for  $e^- \gamma \gamma$  timing. In a first step, the Orange spectrometer is used to scan the electron spectrum and adjust the applied current according to the energy of the conversion electrons (ce). The electron counts were normalized to the beam current. Figure 2 shows scans of the electron spectra for  $^{178}\text{W}$  and  $^{180}\text{W}$

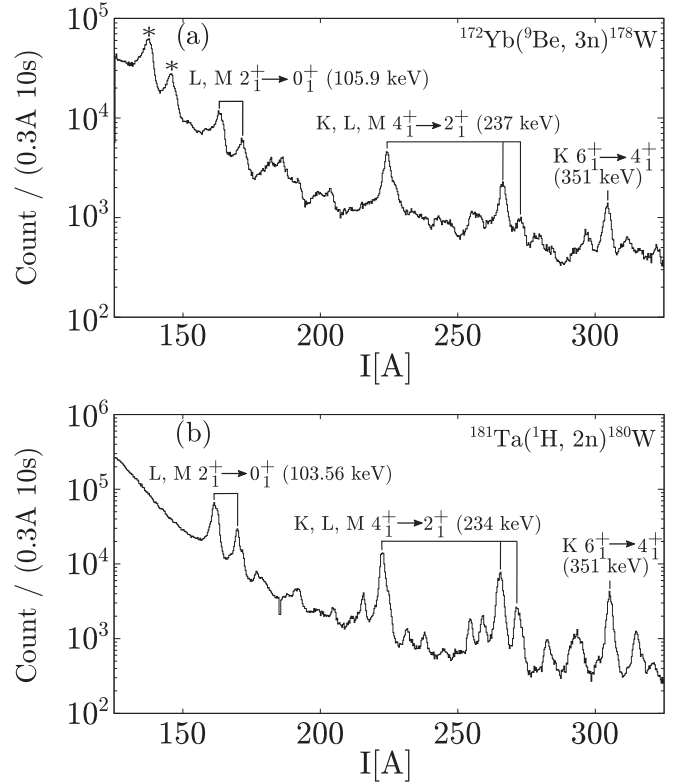


FIG. 2. Conversion electron momentum scans of  $^{178,180}\text{W}$  between 125 and 325 A corresponding to an electron residual energy range of 60 to 310 keV. The scan is performed in steps of 0.3 A with 10-s measurements and the electron counts were normalized to the beam current. The L and M peaks of the  $2^+ \rightarrow 0^+$  transition and the K, L, and M peaks of the  $4^+ \rightarrow 2^+$  of (a) the  $^{178}\text{W}$  reaction and (b) the  $^{180}\text{W}$  reaction are marked. The peaks at 137 and 144 A, marked with asterisks in (a), are the L and M peaks of the  $2^+ \rightarrow 0^+$  transition in  $^{172}\text{Yb}$  from the Coulomb excitation of the target.

between 125 and 325 A corresponding to an electron residual energy of 60 to 310 keV. The K conversion electron lines of the  $2^+ \rightarrow 0^+$  transitions with 105.9 keV for  $^{178}\text{W}$  and 103.6 keV for  $^{180}\text{W}$  are buried in the strong  $\delta$ -electron background. Therefore, the L-peaks of these transitions were used for the timing analysis. The Orange spectrometer was equipped with eight  $1.5'' \times 1.5''$  LaBr<sub>3</sub>(Ce) scintillation detectors (hereafter LaBr) and one high-purity germanium detector (hereafter HPGe) for monitoring purposes. Four of the LaBr detectors were surrounded by bismuth germanate (BGO) scintillators, which are used as an active shield to suppress background from Compton scattering. The LaBr detectors without BGO shields were excluded in the analysis due to high scattering. Effectively, this leads to a further reduction of Compton background in the shielded detectors. The dynode outputs of the LaBr detectors deliver the energy information according to the pulse height. The anode outputs of the LaBr detectors are connected to a constant fraction discriminator (CFD). The timing signals are combined into multiplexed start-stop groups according to Ref. [33] and fed into time-to-amplitude (TAC) converters. The TAC and dynode output signals are connected to a digitizer module [34]. In Figs. 3(b) and 3(c),

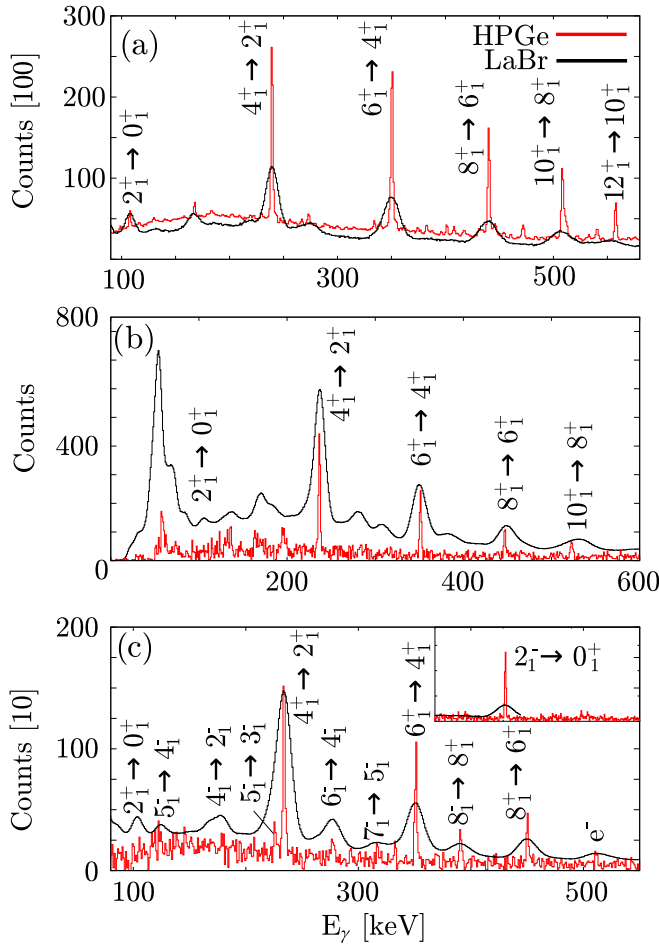


FIG. 3. LaBr spectra and HPGe spectra in coincidence with the  $2_1^+ \rightarrow 0_1^+$  transition (observed with HPGe detectors in HORUS in  $^{176}\text{W}$  and with the Orange spectrometer in  $^{178,180}\text{W}$ ) for (a)  $^{176}\text{W}$ , (b)  $^{178}\text{W}$ , and (c)  $^{180}\text{W}$ . In (a) and (b) the yrast cascade  $\gamma$ -ray lines are marked. In (c) the yrast  $\gamma$ -ray lines as well as some of the  $K^\pi = 2^-$  band  $\gamma$ -ray lines and the  $8_1^- \rightarrow 8_1^+$  transition from the  $K^\pi = 8^-$  band to the ground state band are marked. The small overlay box shows the 902.8 keV  $\gamma$  ray of the  $2_1^- \rightarrow 2_1^+$  transition from the  $K^\pi = 2^-$  band to the ground state band.

the measured LaBr and HPGe spectra for  $^{178,180}\text{W}$  are shown, where the current of the Orange spectrometer was set to 163.5 A (105.9 keV) and 161.5 A (103.6 keV), respectively. A partial level scheme for all three investigated tungsten isotopes in each experiment is shown in Fig. 4. In  $^{176,178}\text{W}$ , the yrast cascade up to the  $10_1^+$  state was detected with enough statistics for the fast-timing analysis. In  $^{180}\text{W}$ , the  $10_1^+$  state was not populated, but negative parity states from the  $K^\pi = 2^-$  octupole rotational band up to the  $7_1^-$  state band were observed [35] as well as the  $8_1^-$  state of the  $K^\pi = 8^-$  band [36].

### B. The HORUS cube spectrometer

The experiment to measure the lifetimes in  $^{176}\text{W}$  using fast timing was conducted at the HORUS cube spectrometer of the IKP Cologne [37]. The spectrometer was equipped with eight HPGe detectors and 10 LaBr fast-timing scintillators. The

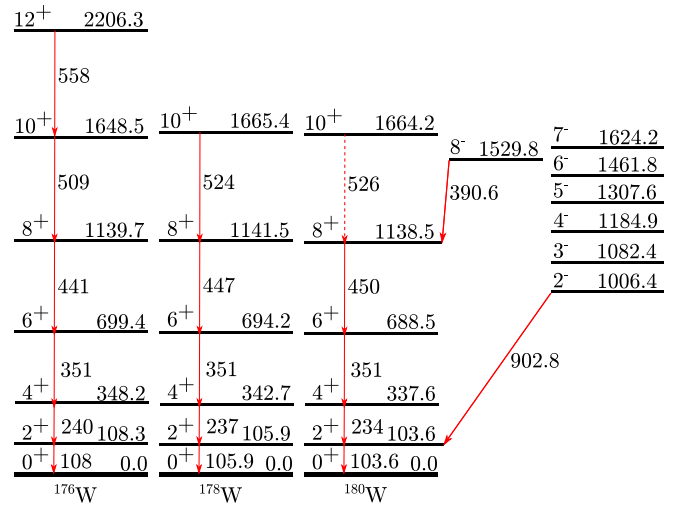


FIG. 4. Relevant level schemes of  $^{176,178,180}\text{W}$ . All transitions depicted with solid lines were used for the lifetime analysis in this work, and are labeled with their respective transition energy. The level and transition energies were adopted from the Nuclear Data Sheets [15–17].

crystals of the LaBr detectors were of two different shapes. Eight  $1.5 \times 1.5$  in.<sup>2</sup> cylindrical crystals and two smaller cone-shaped crystals were used. Six of the LaBr detectors with cylindrical crystals were surrounded by active BGO shields. A schematic drawing of the geometry of this setup is depicted in Fig. 5. This configuration has already been used for several

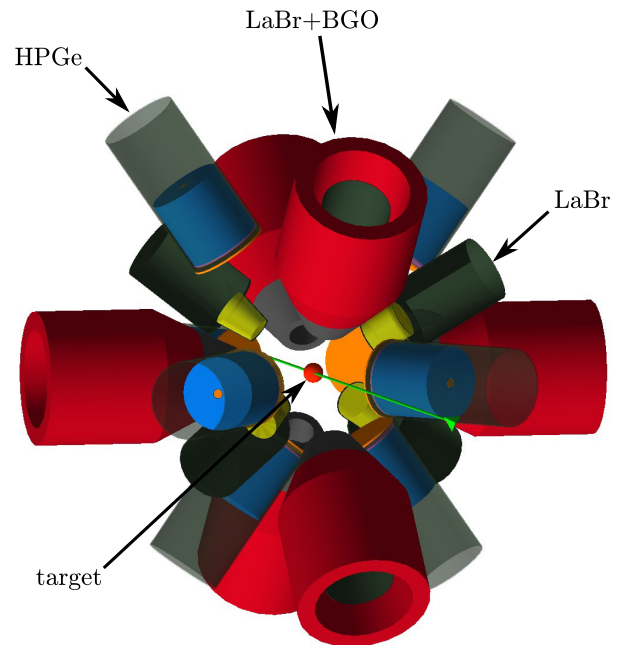


FIG. 5. Schematic drawing of the HORUS setup. The red tubes are the BGO Compton shields, the blue cylinders are the HPGe detectors. The yellow shapes are the LaBr fast-timing scintillators attached to their photo-multiplier tubes, depicted in gray. The beam direction is depicted by a green arrow.

successful fast-timing experiments and its fast-timing capabilities are well tested [38–41].

### C. The IKP plunger experiment

Lifetimes of excited states with  $J^\pi > 2^+$  in  $^{176}\text{W}$  were also measured using the IKP Cologne coincidence plunger setup [9]. The plunger setup was equipped with five HPGe detectors with relative efficiencies between 55% and 80% under a backward angle of  $143^\circ$  relative to the beam axis and one sevenfold Euroball cluster detector [42] mounted under  $0^\circ$  resulting in a ring of six cluster segments under  $34^\circ$  plus the central segment under  $0^\circ$ . The applied target-to-stopper distances were 2, 4, 6, 9, 13, 25, 35, 50, 70, 100, 150, 190, 300, 500, 700, 1000, and  $1500\ \mu\text{m}$  with respect to electrical contact of the foils. The velocity of the  $^{176}\text{W}$  recoil nuclei was determined to be  $v/c = 0.70(1)\%$  using the shifted and unshifted components of the observed yrast cascade transitions from the  $12_1^+$  down to the  $2_1^+$  state in  $^{176}\text{W}$ . The DDCM [20] was used to determine the lifetimes of the  $4^+$ ,  $6^+$ ,  $8^+$ , and  $10^+$  excited yrast states. To minimize feeding contributions from states above as well as unobserved feeders, a gate on the shifted component, that feeds the state of interest, was applied.

## III. LIFETIME ANALYSIS AND RESULTS

### A. Fast-timing analysis

The fast-timing method relies on measuring the time difference between a feeding transition and the decaying transition (either via conversion electron or  $\gamma$  rays) of the state of interest. When a start signal is given by the feeder and the stop signal by the decay, the delayed time distribution is obtained [26,43]:

$$D(t) = n\lambda \int_{-\infty}^t \text{PRF}(t' - t_i) e^{-\lambda(t-t')} dt' + n_r, \quad \lambda = \frac{1}{\tau}, \quad (5)$$

where  $n$  is the number of coincidences in the time distribution,  $n_r$  is the number of background counts, and  $\tau$  is the lifetime of the state connected by the feeder-decay cascade. The delayed time distribution  $D(t)$  is a convolution of the prompt response function (PRF) of the system and an exponential decay.

If the lifetime of a given state is long compared to the full width at half maximum (FWHM) of the PRF, the time difference spectra show an exponential decay as a slope. The slope of the spectrum can be fitted to obtain the lifetime of the exponential decay. If the lifetime of the state of interest is below the resolution of the PRF, they are accessible through the centroid difference method [26,44]. The centroid difference method is based on measuring the centroid  $C$  of delayed ( $d$ ) and antidelayed ( $ad$ ) time distribution where the latter one is obtained by inverting start and stop signals. The lifetime can then be determined according to [26]

$$\tau = \frac{1}{2}(\Delta C - \text{PRD}(E_{\text{feeder}}, E_{\text{decay}})), \quad (6)$$

where  $\Delta C = C_d - C_{ad}$  is the centroid difference and PRD is the prompt response difference that describes the  $\gamma$ - $\gamma$  zero time response of the detector system [26]. The generalization of Eq. (6) for  $N$  detectors is known as the generalized centroid difference (GCD) method [44].

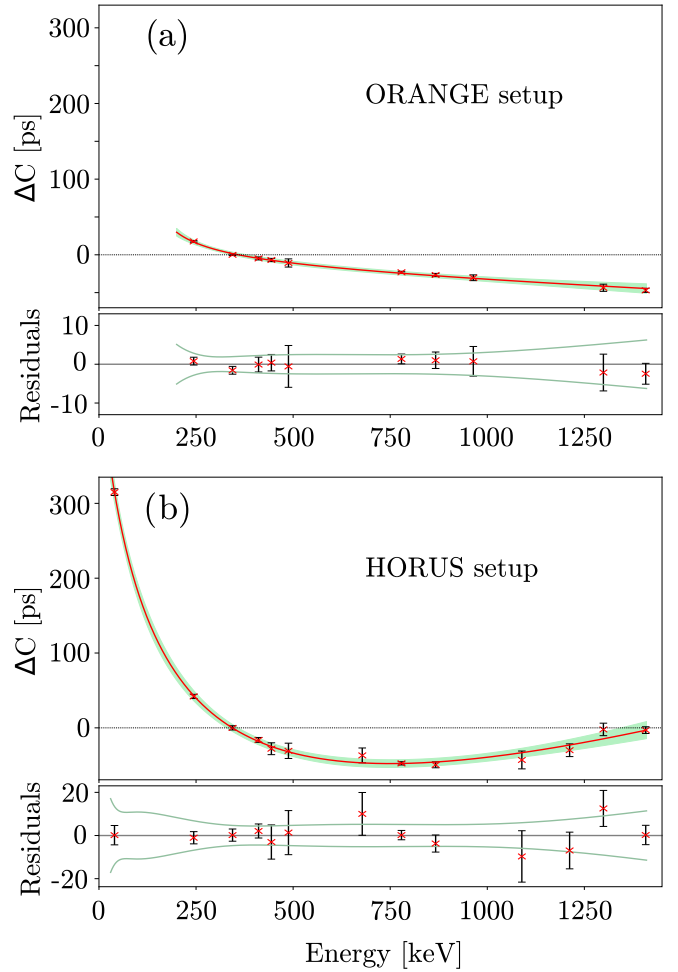


FIG. 6. The PRDs of (a) the Orange setup and (b) the HORUS setup. The upper panels in (a) and (b) show the prompt response difference curve, determined with coincident  $\gamma$  rays from a  $^{152}\text{Eu}$  source at target position. The fitted calibration functions are displayed by the red lines. The uncertainties are displayed by the green uncertainty bands. The zero reference is 344 keV in both cases. The residuals of the PRD fits with uncertainties and  $1\sigma$  interval, displayed by the green lines, are depicted in the lower panels.

The final PRD curves for both setups (HORUS and Orange) were calibrated using  $\gamma$  rays from a  $^{152}\text{Eu}$  source and are fitted using the following function [44]:

$$\text{PRD}(E_\gamma) = \frac{a}{\sqrt{(b - E_\gamma)}} + c + dE_\gamma.$$

Both curves are shown in Fig. 6. The uncertainty of the PRD is not larger than 5 ps in the energy range of interest for both setups. Note that Eq. (6) only holds under the assumption that no background is present. Time correlated background resulting from scattered coincident  $\gamma$  rays has to be corrected for. The procedure is explained in Ref. [44] and was successfully applied in Refs. [38,41,45,46]. In this analysis, the lifetimes of the  $2_1^+$  states in all three tungsten isotopes were determined using the slope method while the higher-lying excited states were measured using the GCD method.

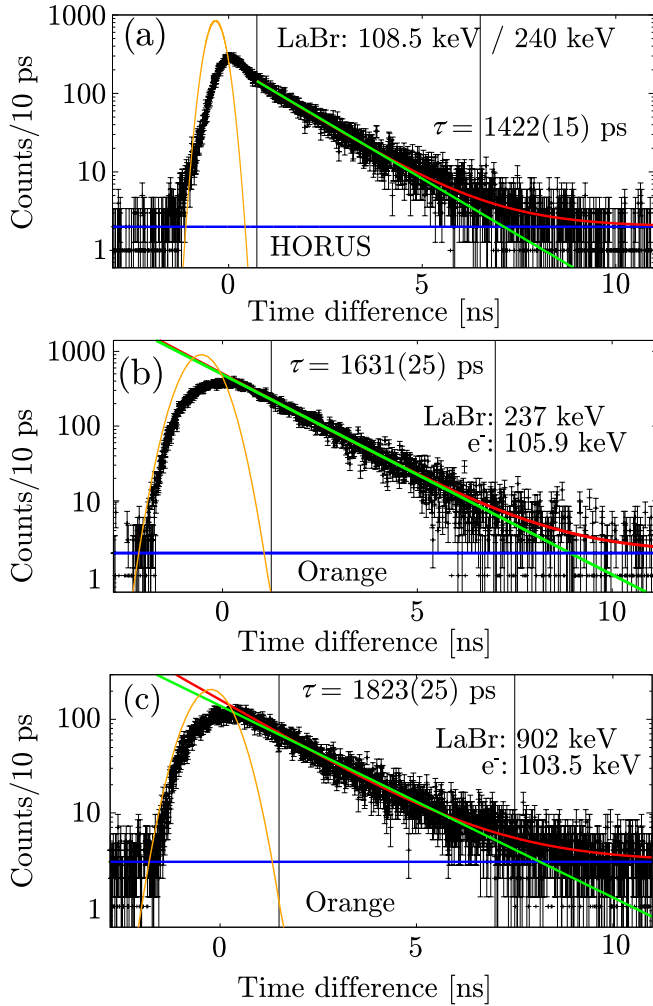


FIG. 7. Time distributions for the  $2_1^+$  states in (a)  $^{176}\text{W}$ , (b)  $^{178}\text{W}$ , and (c)  $^{180}\text{W}$ . The fits to the exponential decay are shown as green lines, the constant background contribution is indicated by blue constants, and the fit with all components by red curves. The fit ranges are indicated by vertical lines. Each panel is labeled with the respective conversion electron and LaBr gates and resulting lifetimes. The yellow centroids are the prompt response functions of the HORUS respective Orange timing systems. The time resolution of the LaBr-Orange timing system is around 1000 ps [22], indicated by the widened PRF, shown in (b) and (c), compared to the LaBr-LaBr timing system of the HORUS spectrometer with a time resolution of about 340 ps.

In Fig. 7(a) the time spectra for the lifetime measurement of the  $2_1^+$  state in  $^{176}\text{W}$  is shown. It is generated by placing a LaBr gate on the  $2_1^+ \rightarrow 0_1^+$  (108.5 keV) transition and another one on the  $4_1^+ \rightarrow 2_1^+$  (240 keV) transition.

The lifetimes of the  $2_1^+$  states in  $^{178,180}\text{W}$  were measured with the Orange spectrometer using  $e^-$ - $\gamma$  coincidences. In Fig. 7(b) the respective time spectrum for the lifetime measurements in  $^{178}\text{W}$ , with one gate on the L1 conversion electron of the  $2_1^+ \rightarrow 0_1^+$  (106 keV) transition and a narrow LaBr gate on the  $4_1^+ \rightarrow 2_1^+$  (237 keV) transition, is shown. The lifetime measurement of the  $2_1^+$  state in  $^{180}\text{W}$  is shown in Fig. 7(c). Here, the gates are placed on the  $2_1^- \rightarrow 2_1^+$  (903

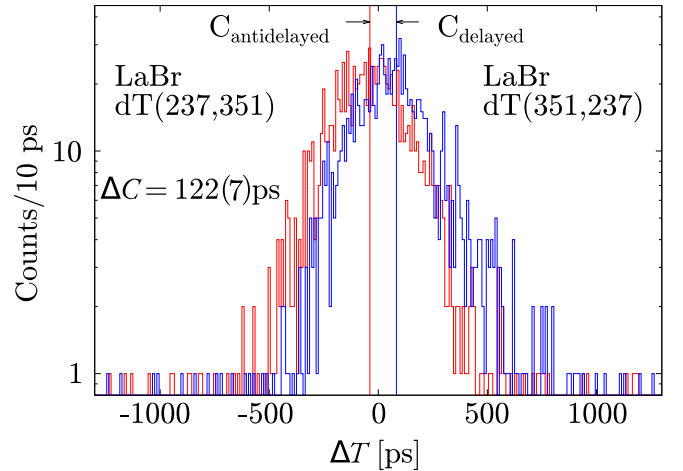


FIG. 8. Centroid difference of the  $6_1^+ \rightarrow 4_1^+ \rightarrow 2_1^+$   $\gamma$  cascade in  $^{178}\text{W}$ , generated using a conversion electron gate on the  $2_1^+ \rightarrow 0_1^+$  transition. Displayed are the time distributions for delayed (blue) and antidelayered (red) gate sequence.

keV) and  $2_1^+ \rightarrow 0_1^+$  (103.6 keV) transitions. Note that the feeding transition was the  $2_1^- \rightarrow 2_1^+$  (903 keV) and not the  $4_1^+ \rightarrow 2_1^+$  transition. The 903 keV transition has considerably less uncorrelated background compared to the 234 keV feeder, as the 234 keV peak has a contamination of the  $5_1^- \rightarrow 3_1^-$  lying in its left flank. For each time spectrum presented in Fig. 7 the corresponding exponential fit to determine the lifetimes is shown. The fit components are depicted by the colored curves: background component in blue, exponential component in green, and the combined fit in red. The final lifetimes result in  $\tau = 1422(15)$  ps for  $^{176}\text{W}$ ,  $\tau = 1631(25)$  ps for  $^{178}\text{W}$ , and  $\tau = 1823(25)$  ps for  $^{180}\text{W}$ . The uncertainties correspond to the maximum deviations of the fits from the median.

The lifetime determination using the HPGe or conversion electron triggered  $\gamma$ - $\gamma$  coincidence measurements is shown as an example for the  $4_1^+$  state in  $^{178}\text{W}$ . Figure 8 shows the delayed and antidelayered time distributions with the  $6_1^+ \rightarrow 4_1^+$  (351 keV) feeding and the  $4_1^+ \rightarrow 2_1^+$  (237 keV) decaying transition, where a trigger has been set on the conversion electron of the  $2_1^+$  decay of 105.9 keV. The centroid difference was measured to be  $\Delta C = 122(7)$  ps. This result has to be corrected for time correlated background underneath the peak of the feeding and the decaying transition. The background underneath the full-energy peak has to be interpolated from centroid difference measurements around the peak of interest according to the standard procedure discussed in Refs. [28,44]. The LaBr and HPGe reference spectra as well as the centroid differences in picoseconds, the background centroid differences, as well as the interpolated background at the respective peak positions for the  $4_1^+$  state are shown in Fig. 9. The interpolated background time response is weighted with the peak-to-background ratio and combined with the PRD value for the energies of the respective feeder-decay cascade; the lifetime of the  $4_1^+$  state, corresponding to  $\tau = 70(5)$  ps, is derived using Eq. (6). This value is consistent with the previously reported result of  $\tau = 65(6)$  ps [18].

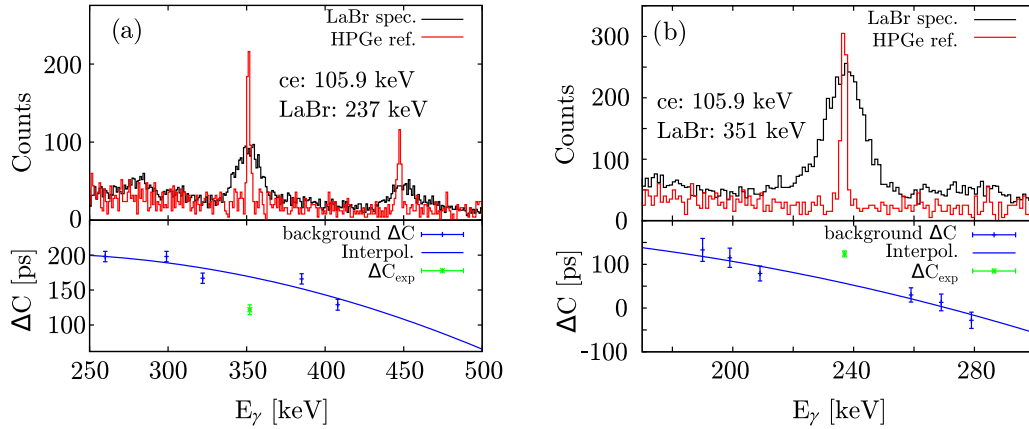


FIG. 9. Analysis of the  $4_1^+$  state of  $^{178}\text{W}$ . In red and black, double gated HPGe and LaBr energy spectra with an Orange trigger gate on the  $2_1^+ \rightarrow 0_1^+$  transition and a LaBr gate on the (a)  $4_1^+ \rightarrow 2_1^+$  (237 keV), which results in an antidelayed time spectrum, and the (b)  $6_1^+ \rightarrow 4_1^+$  (351 keV), which results in a delayed time spectrum. The peaks of interest are well separated from contaminating transitions. In the lower parts of the plots, the measured centroid difference (green) and the measured background time response and corresponding interpolations (blue) are shown.

The lifetimes of the other excited yrast states were determined in the same way with a gate from the next higher-lying yrast state each. Since the  $10_1^+$  state was not excited in  $^{180}\text{W}$ , the lifetime of the  $8_1^+$  state was determined using the  $\gamma$  cascade from the  $8_1^-$  state from the  $K^\pi = 8^-$  band. The experimental results are shown in Table I. The reduced transition probabilities were calculated using the conversion coefficients of the BrIcc database [47] and the transition energies from the evaluated Nuclear Data Sheets [15–17].

### B. RDDS and DDCM analysis

The lifetimes of the  $4_1^+$ ,  $6_1^+$ ,  $8_1^+$ , and  $10_1^+$  yrast states of  $^{176}\text{W}$  were also determined using the RDDS and DDCM. In

Fig. 10 gated spectra of the detectors under the  $143^\circ$  backward angle, with respect to the beam axis, are shown for the  $^{176}\text{W}$  experiment. The gated spectra, shown for different target-to-stopper distances between 2 and 1500  $\mu\text{m}$ , are generated by applying a gate on the  $12_1^+ \rightarrow 10_1^+$  (558 keV) transition. The  $\gamma$ -ray energies of the yrast cascade from the  $4_1^+$  up to the  $10_1^+$  state are marked with two dashed lines, where the dashed line on the left corresponds to the shifted component and the dashed line on the right to the unshifted component. For a distance of 1500  $\mu\text{m}$ , all recoiled nuclei are in flight and all  $\gamma$  rays are entirely Doppler shifted. By lowering the distance between target and stopper an increasing amount of recoiled nuclei are stopped before their  $\gamma$  decay and  $\gamma$  rays not influenced by Doppler shifts are detected. The energetically higher

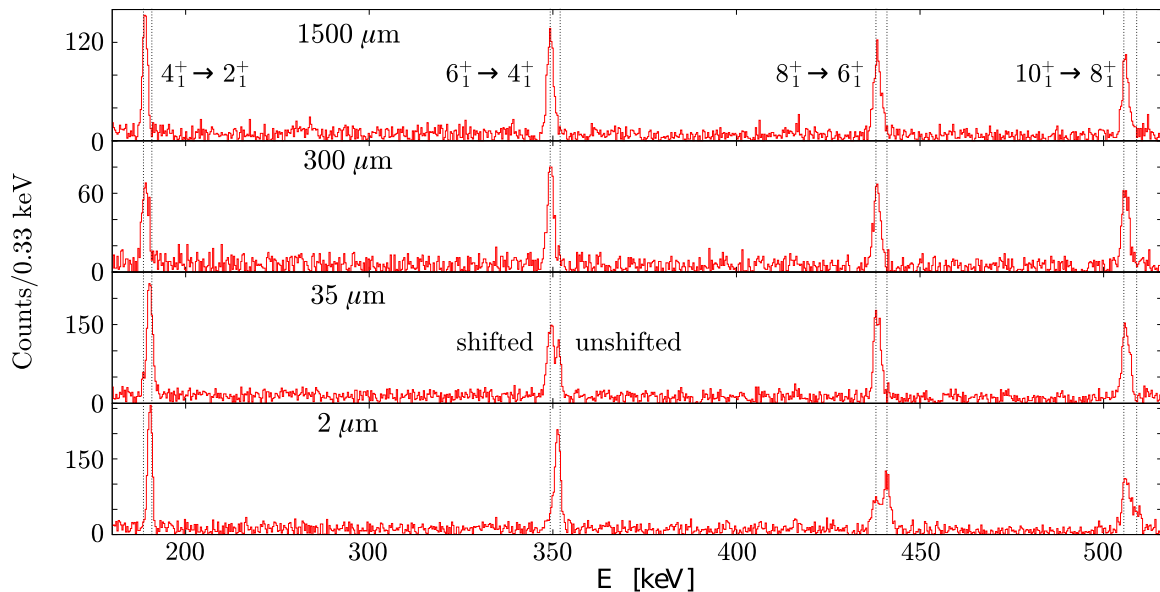


FIG. 10. Projections of the  $\gamma$ - $\gamma$  coincidences with a gate on the flight component of the  $12_1^+ \rightarrow 10_1^+$  transition in  $^{176}\text{W}$  are shown for different target-to-stopper distances under backward angle. Yrast transitions of interest are marked with dashed lines, where the left lines mark the Doppler-shifted and the right ones the unshifted components.

TABLE I. Summary of lifetimes measured in this work and derived reduced transition strengths in comparison adopted literature values and IBM-1 calculations from this work (see Sec. IV B). In the case of  $^{176}\text{W}$ , the values marked with an asterisk are resulting from the plunger experiment from Sec. III B and the unmarked values for  $^{176}\text{W}$  are derived from the HORUS fast-timing experiment. The values printed in bold are adopted for further discussion and the extraction of the  $B(E2)$  values in the case of  $^{176}\text{W}$ . For details on the selection of the adopted values see Sec. III B.

Nucleus	$I^\pi$	$\tau$ (ps)		$B(E2; I^\pi \rightarrow I^\pi - 2)$ (W.u.)		
		This work	Literature	This work	Literature	IBM-1
$^{176}\text{W}$	$2_1^+$	1422(15)	1431(9) <sup>a</sup>	170(3)	166(3) <sup>a</sup>	170
	$4_1^+$	<b>57.9(29)</b> 64.2(12)*		258(13)		244
	$6_1^+$	10.7(30) <b>8.1(3)*</b>		306(11)		270
	$8_1^+$	<8 <b>3.8(5)*</b>		213(24)		281
	$10_1^+$	<b>2.1(4)*</b>		$190^{+44}_{-30}$		283
$^{178}\text{W}$	$2_1^+$	1631(25)	1642(21) <sup>b</sup>	154(3)	153(2) <sup>b</sup>	154
	$4_1^+$	70(4)	65(6) <sup>c</sup>	$222^{+13}_{-12}$	$238^{+24}_{-18}$ <sup>c</sup>	224
	$6_1^+$	9.8(38)	<14.4 <sup>c</sup>	$230^{+134}_{-64}$	>170	254
	$8_1^+$	<6		>105		>269
	$2_1^+$	1823(25)	1850(70) <sup>d</sup>	141(3)	139(6)	141
$^{180}\text{W}$	$4_1^+$	79.4(29)		204(7.7)		208
	$6_1^+$	12(3.5)		$199^{+82}_{-45}$		234
	$8_1^+$	<8.6		>74		>247

<sup>a</sup>Reference [22].

<sup>b</sup>Reference [18].

<sup>c</sup>Reference [19].

<sup>d</sup>Reference [17].

peaks are not entirely stopped, because the time of flight of the recoiled nuclei tends to be longer than the lifetime of the respective state. But even at the lowest distance of 2  $\mu\text{m}$ ,

both components can be observed. Note that the peaks of the  $4_1^+ \rightarrow 2_1^+$  transition are not well separated. The reason is the relatively low velocity ( $\frac{v}{c} \approx 0.7\%$ ) of the recoiled reaction product of the specific fusion evaporation reaction. Due to nearly indistinguishable shifted and unshifted components of the  $4_1^+ \rightarrow 2_1^+$  transition, as visible in Fig. 10, the lifetime measurement using the RDDS method or DDCM does not generate a reasonable result. The given uncertainty does only reflect the statistical error and not the systematic error of the poorly separated shifted and unshifted components. Thus, the lifetime of the fast-timing experiment is used for further discussions about the  $4_1^+$  state. The separation of the shifted and unshifted components of the decaying transitions of the  $6^+$ ,  $8^+$ , and  $10^+$  states is sufficient and can be used to determine lifetimes. With the applicability limit of the fast-timing method being around 10 ps [26] the results of the plunger method have been used for further discussions about the yrast states with  $J^+ > 4^+$ . In Table I, the results of the plunger experiment in the case of  $^{176}\text{W}$  are indicated by asterisks. The results for  $^{176}\text{W}$  used for further discussions and the extraction of the  $B(E2)$  values are printed in bold text in Table I.

Figure 11 shows an example of the DDCM analysis for the lifetime determination of the  $6_1^+$  state, gated on the flight components of the indirect feeding  $10_1^+ \rightarrow 8_1^+$  [Fig. 11(a)] and  $12_1^+ \rightarrow 10_1^+$  in forward [Fig. 11(b)] and backward angle [Fig. 11(c)]. The lifetimes of the  $6^+$ ,  $8^+$ , and  $10^+$  states in  $^{176}\text{W}$  were determined according to the example shown in Fig. 11. A summary of the determined lifetimes including gate information and adopted values is shown in Table II.

## IV. DISCUSSION

### A. Systematic of $B(E2)$ values and quadrupole deformation

Collective signatures in atomic nuclei can be described by different parameters like the  $R_{4/2} = E_{4_1^+}/E_{2_1^+}$  ratio greater than 2 or  $B(E2; 2^+ \rightarrow 0^+)$  values larger than 10–20 W.u. [49]. Further parameters are, e.g., intrinsic electric quadrupole

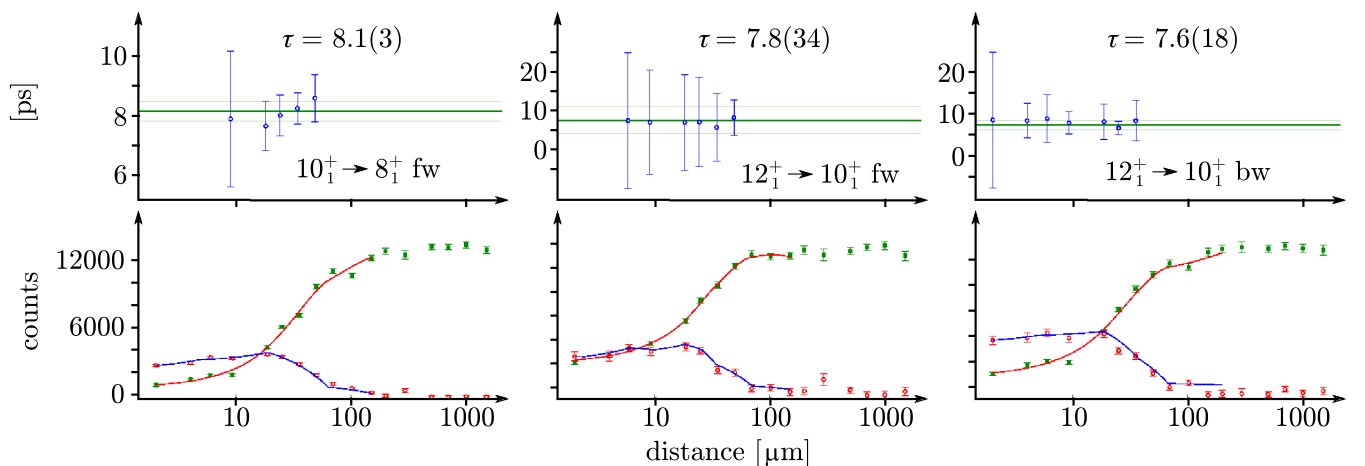


FIG. 11. Example of the DDCM analysis for the  $6_1^+$  state using the software NAPATAU [48]. The upper panels show the corresponding obtained lifetimes. The lower panels show the evolution of the shifted component intensities (green data points and red curves) and derivatives (light red data points and blue curves). The  $\tau$  plots are depicted with their corresponding gate configurations and angles, where “fw” means forward angle and “bw” means backward angle.

TABLE II. Summary of the determined lifetimes in  $^{176}\text{W}$  from the RDDS experiment with respective gates and weighted means. Forward and backward angles are marked with “fw” and “bw,” respectively. The weighted means of each lifetime are printed in bold text.

Gate	$4_1^+$	$\tau$ (ps)	Gate	$6_1^+$	$\tau$ (ps)
$8_1^+ \rightarrow 6_1^+$ fw		64.3(14)	$12_1^+ \rightarrow 10_1^+$ fw		7.8(34)
$8_1^+ \rightarrow 6_1^+$ bw		67.7(21)	$12_1^+ \rightarrow 10_1^+$ bw		7.6(18)
$6_1^+ \rightarrow 4_1^+$ fw		62.9(12)	$10_1^+ \rightarrow 8_1^+$ fw		8.1(3)
<b>Weighted mean</b>		<b>64.2(12)</b>	<b>Weighted mean</b>		<b>8.1(3)</b>
Gate	$8_1^+$	$\tau$ (ps)	gate	$10_1^+$	$\tau$ (ps)
$10_1^+ \rightarrow 8_1^+$ bw		3.7(7)	$12_1^+ \rightarrow 10_1^+$ bw		1.9(12)
$12_1^+ \rightarrow 10_1^+$ fw		3.9(6)	$8_1^+ \rightarrow 6_1^+$ bw		2.1(4)
<b>Weighted mean</b>		<b>3.8(5)</b>	<b>Weighted mean</b>		<b>2.1(4)</b>

moment  $Q_0$ , deformation parameter  $\beta$ , and the  $B_{4/2} = B(E2; 4_1^+ \rightarrow 2_1^+)/B(E2; 2_1^+ \rightarrow 0_1^+)$  ratio which is expected to be 1.43 for a heavy deformed nucleus [49]. The experimental data obtained in this work enable a more complete picture of the evolution of the collective signatures of the tungsten isotopes around the rare-earth neutron midshell at  $N = 104$ . As can be seen in Fig. 12(a), the tungsten isotopes around the neutron midshell show an increasing  $R_{4/2}$  ratio with a maximum at  $^{182}\text{W}_{108}$ . The ratio increases from around 2.9 at  $N = 94, 96$  to 3.29 for  $N = 108$ . For the near-midshell isotopes this suggests the interpretation of close to axially symmetric rigid rotors which have theoretical  $R_{4/2}$  ratios of 3.33 [10]. Looking at Figs. 12(a) and 13 (top), it is clear that most isotopes have exceeded the X(5) limit of  $R_{4/2} = 2.91$ , but for the lighter tungsten isotopes, this signature indicates slight hints of X(5) characteristics. The  $B(E2)$  values of the  $2_1^+ \rightarrow 0_1^+$  and  $4_1^+ \rightarrow 2_1^+$  transitions are shown in Fig. 12(b). In this mass region, the increasing  $B(E2, 2_1^+ \rightarrow 0_1^+)$  values as a function of decreasing neutron number are commonly interpreted as an increase in collectivity towards more neutron-deficient nuclei. A saturation of collectivity around  $N = 100$  to neutron midshell  $N = 104$  can be assumed, based on the current  $B(E2)$  data. The evolution of the newly acquired  $B(E2; 4_1^+ \rightarrow 2_1^+)$  values accompanies the evolution of the  $B(E2; 2_1^+ \rightarrow 0_1^+)$  values depending on the neutron number. Both evolutions follow a similar general tendency. Though the maximum of both signatures,  $B(E2; 2_1^+ \rightarrow 0_1^+)$  and  $B(E2; 4_1^+ \rightarrow 2_1^+)$ , lies near midshell, as expected in well-deformed nuclei, a satisfactory explanation for the displaced maximum of the  $B(E2)$  values towards neutron-deficient isotopes is not yet presented.

Compared to the lighter even-even hafnium, ytterbium, and erbium neighbors with  $Z = 72, 70,$  and  $68$ , a similar behavior of the  $B(E2)$  values of the low-spin yrast states is found. In these isotopes the  $B(E2; 2_1^+ \rightarrow 0_1^+)$  value peaks at  $N = 100, N = 102,$  and  $N = 98$ , respectively, emphasizing the saturation of collectivity in this region when approaching the midshell [24,55], but with slight displacement to the neutron-deficient side. This effect of pre-midshell saturation could partly be caused by the influence of the hexadecapolar

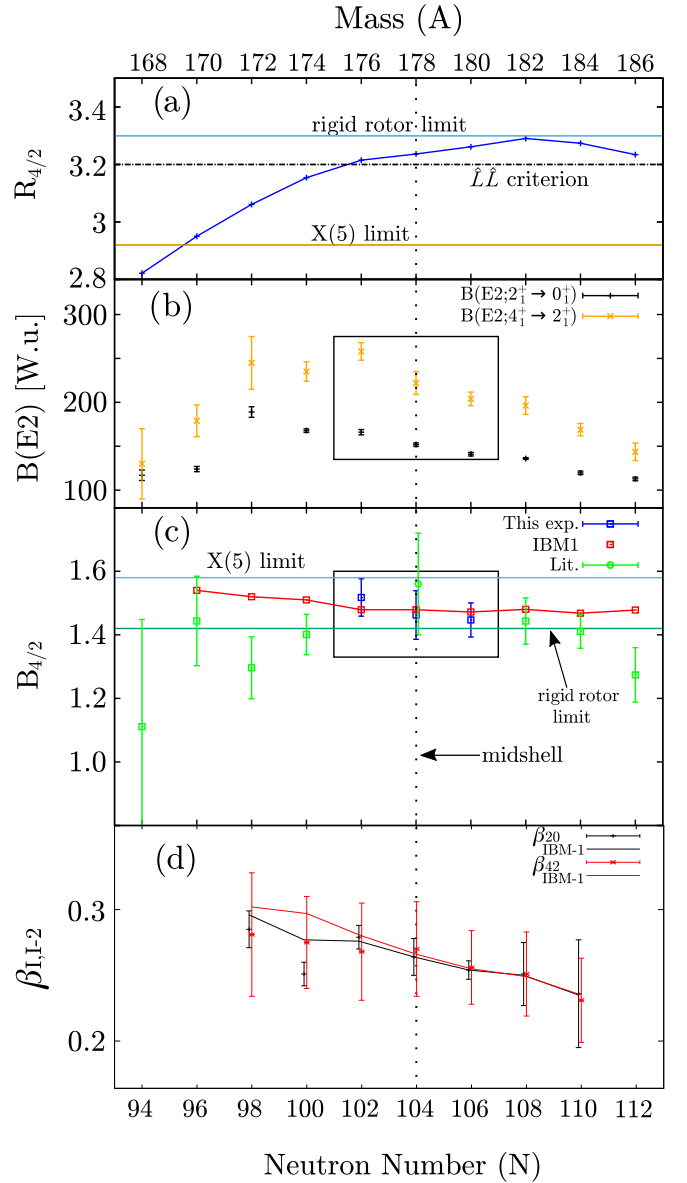


FIG. 12. The evolution of (a)  $R_{4/2}$  ratios, (b)  $B(E2)$  values, (c)  $B_{4/2}$  ratios, and (d) experimental quadrupole deformation parameters of the tungsten isotopes around  $N = 104$  compared with the IBM-1 calculations from this work. The  $\beta$  values obtained from the IBM-1 calculations are drawn with solid lines in the same color as the experimental values. Experimental values for the energies and the literature values of the  $B(E2)$  values are taken from Refs. [15–17,19,50–54]. Rigid rotor and X(5) limits are shown as horizontal lines. The  $\hat{L}\hat{L}$  criterion as mentioned in Sec. IV B is displayed as a dashed line in (a).

deformation  $\beta_4$  on the quadrupole moment  $Q_2$ , as proposed in Ref. [56], investigated and discussed for this region in Refs. [18,55]. A detailed study of the hexadecapolar deformation  $\beta_4$  for this mass region, including the tungsten isotopes, is presented in Ref. [55]. This approach, however, cannot explain the displacement entirely [55].

Figure 12(c) shows the evolution of the  $B_{4/2}$  ratio around the neutron midshell. The ratio is expected to be around

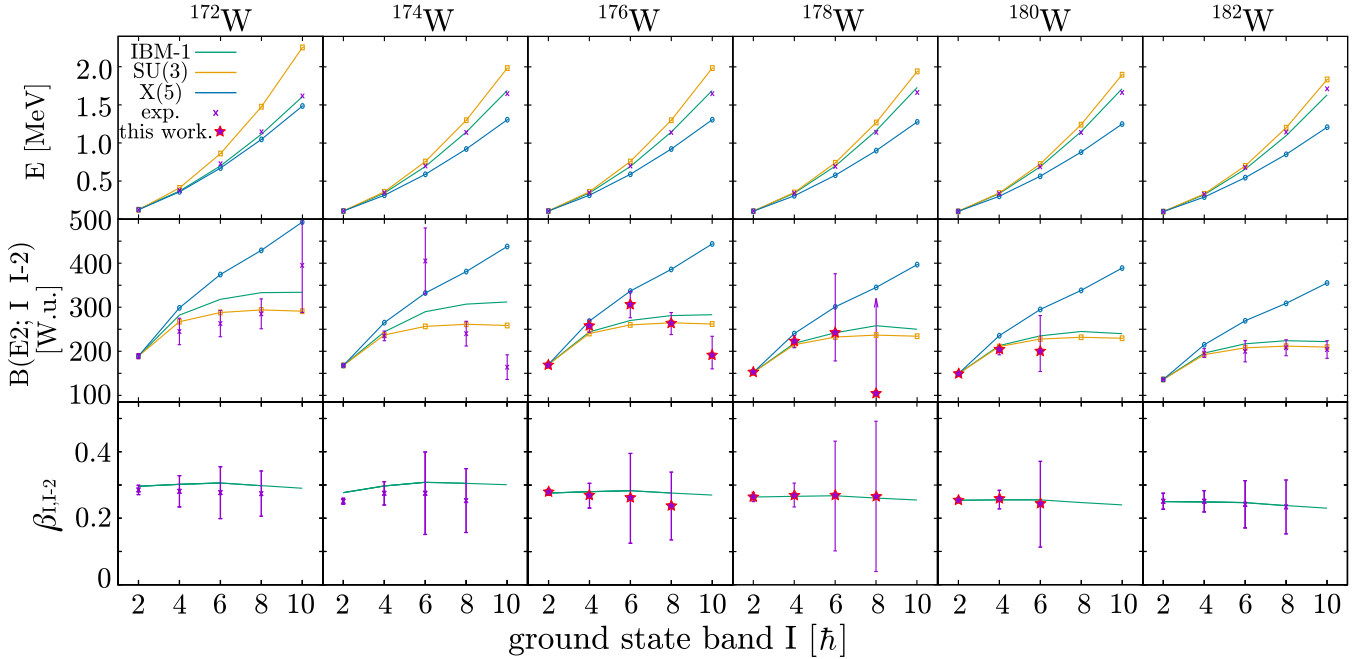


FIG. 13. Excitation energies (top), reduced transition probabilities (middle), and experimental quadrupole deformation parameters  $\beta_{I,I-2}$  (bottom) as a function of yrast spin for  $^{172-182}\text{W}$ . The upper and the middle panels compare the experimental values to the IBM-1 calculations from Sec. IV B and the SU(3) and X(5) limits. The bottom plot compares the experimental values to the IBM-1. The literature values are taken from Refs. [50,52,64,65].

1.428 for well-deformed nuclei, according to the predictions of the rigid rotor model [57] and the SU(3) limit of the interacting boson model [10,25]. In the tungsten isotopes with  $N = 94-110$ , the  $B_{4/2}$  ratio increases from 1.11(34) at  $^{168}\text{W}$  ( $N = 94$ ) towards 1.51(5) at  $^{176}\text{W}$  ( $N = 102$ ) and decreases to 1.41(5) at  $^{184}\text{W}$  ( $N = 110$ ). This increasing behavior towards midshell seems anomalous for isotopic chains in this region. In comparison, the  $B_{4/2}$  ratio decreases in the even-even hafnium and ytterbium neighbors towards midshell to about 1.43 [24,58]. In contrast, the  $B_{4/2}$  ratio of the heavier osmium and platinum isotopes also increases towards midshell starting from very small  $B_{4/2}$  ratios of approximately or smaller than 1 in the very neutron-deficient isotopes, comparable to the  $B_{4/2}$  of the tungsten isotopes [59].

All in all, the simple rotor explanation for the isotopes in this region does not seem to be fully sufficient in the tungsten isotopes. Several indications are observed that suggest a rising of previously unaccounted effects (or at least an uncommon combination of already known effects, as for example the backbending phenomenon [60–62], the hexadecapolar deformation [55], or possibly a shape coexistence phenomenon [63]) in this region: the displacement of the saturation of the  $B(E2)$  values away from midshell towards lighter isotopes [Fig. 12(b)], the displacement of the maximum of the  $R_{4/2}$  ratio away from midshell towards heavier isotopes [Fig. 12(a)], the unexpected behavior of the  $B_{4/2}$  ratios and its very small value at  $^{168}\text{W}$  of 1.11(34) [Fig. 12(c)], as well as the unexpected behavior of the tendency of the  $B(E2)$  values throughout the  $2^+ - 10^+$  yrast states of  $^{174,176}\text{W}$  (see Fig. 13, middle panel). Further experiments and calculations are required to explain this combination of observations.

However, most of the  $B_{4/2}$  ratios considered ( $N = 94-112$ ) agree within their uncertainties with the Alaga rule of 10/7 largely supporting the deformed character as expected from the  $R_{4/2}$  ratio near midshell.

All  $B_{4/2}$  values of the tungsten isotopes are separated from the X(5) limit of 1.58 [6]. Especially for  $^{178}\text{W}$  ( $N = 104$ ) the new results reduced the uncertainties of the  $B_{4/2}$  ratio and there is no overlap with the X(5) limit any more. As Fig. 12(c) reveals, the uncertainty of the  $B_{4/2}$  ratio for  $^{176}\text{W}$  lies very close to the X(5) limit. But the  $R_{4/2}$  ratio contradicts the assumption of a possible X(5) nucleus. Still, the  $B_{4/2}$  ratio as well as the trend of  $B(E2)$  values up to  $B(E2; 6_1^+ \rightarrow 4_1^+)$  (see Fig. 13), with respect to the new experimental data, can be interpreted as following the trend suggested by X(5). But considering all signatures,  $R_{4/2}$ ,  $B_{4/2}$ , and the evolution of the yrast  $B(E2)$  strengths,  $^{176}\text{W}$  agrees certainly more with the SU(3) limit. But the unexpected drop of the  $B(E2)$  values of the  $8_1^+ \rightarrow 6_1^+$  and  $10_1^+ \rightarrow 8_1^+$  transitions seems to be outside the scope of the models. The same effect is observed for the evolution of the  $B(E2)$  values in  $^{174}\text{W}$ . But due to the large uncertainty of the  $B(E2; 6_1^+ \rightarrow 4_1^+)$  value, the situation cannot be fully quantified.

The graphics in Figs. 12(b), 12(c) and 13 including the newly determined values add to the systematic evolution of the  $B(E2)$  values in the neutron midshell region of the tungsten isotopes around  $N = 104$ .

From the deduced  $B(E2)$  values, transitional quadrupole moments  $Q_t$  are calculated according to [49]

$$Q_t(J_i \rightarrow J_f) = \sqrt{\frac{16\pi}{5} \frac{B(E2; J_i \rightarrow J_f)}{\langle J_i K_i 2(\Delta K) | J_f K_f \rangle^2}}, \quad (7)$$

TABLE III. Experimental quadrupole moments and quadrupole deformation parameters  $\beta$  for the  $2_1^+ \rightarrow 0_1^+$ ,  $4_1^+ \rightarrow 2_1^+$ , and  $6_1^+ \rightarrow 4_1^+$  transitions for the tungsten isotopic chain. The  $Q_i$  values were calculated with Eq. (7), the  $\beta$  values with Eq. (8) using  $B(E2)$  values which were taken from this work and from the Nuclear Data Sheets [18,50–53].

Nucleus	$N$	$Q_{20}$	$\beta_{20}$	$Q_{42}$	$\beta_{42}$	$Q_{64}$	$\beta_{64}$
$^{172}\text{W}$	98	7.38(8)	0.28(3)	7.0(12)	0.28(5)	6.9(19)	0.28(8)
$^{174}\text{W}$	100	6.97(5)	0.249(8)	6.9(9)	0.27(4)	8.7(31)	0.35(12)
$^{176}\text{W}$	102	6.9(5)	0.279(2)	6.8(9)	0.27(4)	6.6(34)	0.26(13)
$^{178}\text{W}$	104	6.74(6)	0.26(3)	6.8(9)	0.27(4)	6.8(32)	0.27(16)
$^{180}\text{W}$	106	6.54(5)	0.253(5)	6.6(7)	0.26(3)	6.2(33)	0.24(12)
$^{182}\text{W}$	108	6.47(5)	0.249(2)	6.5(9)	0.25(3)	6.3(18)	0.24(7)
$^{184}\text{W}$	110	6.12(5)	0.234(2)	6.0(9)	0.23(3)	6.0(9)	0.23(4)

where  $\langle J_i K_i 2(\Delta K) | J_f K_f \rangle$  are the Clebsch-Gordan coefficients for transitions from  $J_i$  to  $J_f$  [49], where  $K$  represents the projection of the intrinsic angular momentum on the symmetry axis. The quadrupole deformation  $\beta$  is related to  $Q_i$  via

$$\beta = \frac{\sqrt{5\pi}}{3ZR^2e} Q_i, \quad (8)$$

where  $R = 1.2 \text{ fm } A^{\frac{1}{3}}$  is an approximation for the nuclear radius. The values are calculated for the tungsten isotopes between  $N = 98$  and  $N = 110$  and are given in Table III. Derived from the values in Table III, the quadrupole moments as well as the quadrupole deformation decreases from  $\beta_{20} = 0.28(3)$  in  $^{172}\text{W}$  to  $\beta = 0.234(2)$  in  $^{184}\text{W}$ . The evolution of the quadrupole deformation values  $\beta_{20}$  and  $\beta_{42}$  is depicted in Fig. 12(d) throughout the isotopic chain. Figure 13 (bottom panel) shows nearly constant quadrupole deformation for all yrast states with  $J^+ = 2^+, 4^+, 6^+, \text{ and } 8^+$  for the tungsten isotopes. All  $\beta$  values lie in a typical range expected for a well-deformed rotor [49]. The quadrupole deformation does not suggest a major change in structure in this isotopic chain.

The newly determined data concerning  $^{176,178,180}\text{W}$  complete the experimental database of observables relevant for the discussion of deformation phenomena. The current interpretation does not change significantly; still, the new experimental data yield an argument to support the previous assumptions for the deformation characteristics of the tungsten isotopes  $^{176,178,180}\text{W}$ . But further efforts as experiments and adjustments of the nuclear models are required to reproduce a detailed general description of the data throughout the tungsten isotopic chain.

### B. IBM-1 calculations

To describe the experimental data, theoretical calculations in the framework of the interacting boson model 1 (IBM-1), where no distinction between protons and neutrons is made [66], were performed. In the IBM-1, one assumes that low-lying collective quadrupole states can be generated as states of a system of  $N$  bosons able to occupy two levels, one with angular momentum  $J = 0$ , called  $s$  bosons, and one with angular momentum  $J = 2$ , called  $d$  bosons [67]. In the calculations, only  $s$  and  $d$  bosons are used. The ex-

TABLE IV. The fit parameters for the ECQF Hamiltonian and resulting  $e_{\text{eff}}$  values in  $e b$ .

Nucleus	$\epsilon$	$\kappa$	$\chi$	$\lambda$	$e_{\text{eff}} (e b)$
$^{172}\text{W}^a$	0.520	-0.0154	-1.013	0.0	0.16881
$^{174}\text{W}^a$	0.553	-0.0156	-0.947	0.0	0.14950
$^{176}\text{W}^a$	0.593	-0.0158	-0.946	0.0	0.14758
$^{178}\text{W}^a$	0.615	-0.0157	-0.938	0.0006 <sup>b</sup>	0.12368
$^{180}\text{W}$	0.540	-0.0160	-0.865	0.0011	0.12812
$^{182}\text{W}$	0.500	-0.0169	-0.845	0.0016	0.13649
$^{184}\text{W}$	0.435	-0.0166	-0.800	0.0036	0.14539
$^{186}\text{W}$	0.415	-0.0170	-0.800	0.0046	0.14655

<sup>a</sup>Calculations done by Rudigier *et al.* [18].

<sup>b</sup>The  $\lambda$  value for  $^{178}\text{W}$  was added in this work.

tended consistent Q formalism (ECQF) [68] represents the IBM-1 with only few parameters which has proven to contain the essential physics ingredients to describe the low-lying states in even-even nuclei ranging from vibrational nuclei up to well-deformed rotational nuclei [69,70]. The following Hamiltonian is applied [68]:

$$\hat{H}_{\text{ECQF}} = \epsilon \hat{n}_d + \kappa \hat{Q}^x \cdot \hat{Q}^x + \lambda \hat{L} \cdot \hat{L}, \quad (9)$$

where

$$\begin{aligned} \hat{Q}^x &= (s^\dagger \tilde{d} + d^\dagger s)^{(2)} + \chi (d^\dagger \tilde{d})^{(2)}, \\ \hat{L} &= \sqrt{10} (d^\dagger \tilde{d})^{(1)}, \text{ and} \\ \hat{n}_d &= d^\dagger \cdot \tilde{d}. \end{aligned} \quad (10)$$

The quadrupole operator  $\hat{Q}^x$  is related to the  $E2$  transition probability  $T(E2)$  via the effective boson charge  $e_{\text{eff}}$  according to

$$T(E2) = e_{\text{eff}} Q. \quad (11)$$

The  $\hat{L} \cdot \hat{L}$  term corresponds to the  $\hbar^2/2I$  parameter of the collective model with  $I$  the moment of inertia and determines the  $L(L+1)$  dependence of the energies in the rotational bands.  $\hat{L}$  denotes the boson angular momentum operator [71]. The physics of the  $\hat{L} \cdot \hat{L}$  term is best seen in the pure rotational SU(3) limit of the IBM-1.

The calculations were performed using the computer code ARBMODEL [72]. The calculations were fitted to the level energies from  $2_1^+$  to  $10_1^+$  and level energies of the first three to four states of the  $\gamma$  and  $\beta$  bands, if available, and the  $B(E2; 2_1^+ \rightarrow 0_1^+)$  value. All level energies were taken from the Nuclear Data Sheets [15–17,50,52–54,64,73]. The fits yield the parameters displayed in Table IV. An IBM-1 calculation for the  $^{172,174,176,178}\text{W}$  isotopes is presented by Rudigier *et al.* in Ref. [18], where the influence of the  $\hat{L}\hat{L}$  term was not taken into account. Since the heavier tungsten isotopes  $^{182,184,186}\text{W}$  experience a strong increase of the level energies especially of the higher-lying yrast levels, the band structure could only be reproduced well by taking a small contribution of the  $\hat{L}\hat{L}$  term into account. Following Nomura *et al.* [71] this becomes evident for strongly deformed axially symmetric nuclei. Nomura *et al.* formulate  $R_{4/2} > 3.2$  as a criterion for taking the  $\hat{L}\hat{L}$  term into account. This criterion is displayed as a dashed line

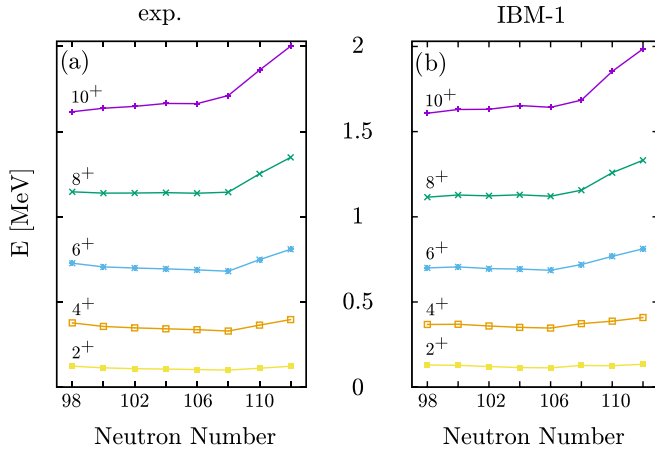


FIG. 14. (a) Experimental and (b) theoretical (IBM-1) level energies of the low-lying yrast  $2^+$ ,  $4^+$ ,  $6^+$ ,  $8^+$ , and  $10^+$  states as a function of the neutron number.

in Fig. 12(a). The parameters for  $^{178}\text{W}$ , originally calculated in Ref. [18], were supplemented by a very small  $\hat{L}\hat{L}$  contribution, indicated by footnote b in Table IV, which leads to a better reproduction of the yrast states. As can be seen in Table IV, the amounts of  $\lambda$  increase slightly with the neutron number.

The results of the calculations of the excitation energies of the yrast states are shown in Fig. 14 together with the experimental values for the tungsten isotopes. The calculated energies show an overall consistency with the measured energies. The highest deviation of the calculations from the experiments in the yrast band in all isotopes was about 20 keV. The effective boson charge was chosen to match the experimental  $B(E2; 2_1^+ \rightarrow 0_1^+)$  values and varies from  $e_{\text{eff}} = 0.12$ -0.14.

The  $B_{4/2}$  ratio of the calculated reduced transition probabilities are shown in Fig. 12(c) in comparison with the experimental values. The resulting  $B_{4/2}$  values match the experimental ones within uncertainties for  $N = 102$  ( $^{176}\text{W}$ ) to  $N = 110$  ( $^{184}\text{W}$ ) but disagree for  $N = 98, 100$ , and 112. According to the model, the  $B_{4/2}$  values of all isotopes considered in the calculations lie close to the SU(3) limit of  $B_{4/2} \approx 1.43$ , similar to what is expected from the experimental values and the  $R_{4/2}$  ratios. Note the opposite movement of the experimental values of  $B_{4/2}$  compared to the model predictions and to the evolution of the  $B_{4/2}$  ratios of the neighbors with fewer protons, hafnium and ytterbium [24,58]. It should be taken into account that the adopted  $B_{4/2}$  value for  $^{172}\text{W}_{98}$  shows a large uncertainty. A reevaluation of this nucleus would be favorable to get a clearer picture of deformation and collectivity in the light tungsten isotopes.

In Fig. 13 the level energies (top) of the first yrast states and corresponding  $E2$  transition strengths (middle) are shown for the midshell tungsten isotopes. While the level energies are clearly approaching the SU(3) limit when adding neutrons, the  $B(E2)$  values do not show a totally clear structure for the midshell tungsten isotopes except for  $^{182}\text{W}$ . The  $B(E2; 6_1^+ \rightarrow 4_1^+)$  value of  $^{180}\text{W}$  and the  $B(E2; 8_1^+ \rightarrow 6_1^+)$  value of  $^{178}\text{W}$  show large uncertainties, as the lifetimes are almost at the lower boundary of the sensitivity of the fast-timing method,

and do not allow for a clear interpretation. However, within the uncertainties, they confirm the interpretation of axially symmetric prolate rotors as they are consistent with the SU(3) limit and the IBM-1 calculations. Although the excitation energies show a rotorlike structure for  $^{174,176}\text{W}$ , the  $B(E2)$  values do not allow a clear interpretation of rotational structure within the uncertainties, as described in Sec. IV A. The IBM-1 calculations place the  $B(E2)$  values of these two isotopes close to SU(3), but the experimental values for  $B(E2; 6_1^+ \rightarrow 4_1^+)$  and  $B(E2; 10_1^+ \rightarrow 8_1^+)$  show deviations from this model. The general tendency of the  $B(E2)$  values is not described by the IBM-1 for  $^{176}\text{W}$  and also  $^{174}\text{W}$ . There are significant deviations from all models for the reduced transition probabilities for these transitions (see Fig. 13, middle panel). This suggests the large deviations for the  $E2$  transitions in  $^{174}\text{W}$  and  $^{176}\text{W}$  to be a signature of a structural change within the yrast band, especially with respect to the evolution towards very unusual  $B_{4/2}$  values of the extremely neutron-deficient nuclei of, e.g.,  $B_{4/2} = 0.33(8)$  for  $^{166}\text{W}$  [74], that cannot be explained with any model so far. Using an extension of the IBM-1, allowing for multiple two particle–two hole excitation, might account for this observation [61,62]. Such a description involves many more parameters to be fitted to higher spin states. This as well as a further development of the nuclear models is considered to be outside the scope of this work.

## V. SUMMARY

Lifetimes of yrast states in the midshell tungsten isotopes with  $A = 176, 178, 180$  have been measured using fast-timing methods with  $e^-$ - $\gamma$ - $\gamma$  and  $e^-$ - $\gamma$  coincidences at the Orange spectrometer setup, HPGe triggered  $\gamma$ - $\gamma$ - $\gamma$  coincidences using the HORUS cube spectrometer, and the RDDS technique in combination with the DDCM. Lifetimes of the  $2_1^+$  states in all three isotopes as well as  $4_1^+$  and  $6_1^+$  in  $^{178}\text{W}$  have been remeasured. Lifetimes of the  $4_1^+$ ,  $6_1^+$ , and  $8_1^+$  states have been measured in all isotopes and additionally the lifetime of the  $10_1^+$  state in  $^{176}\text{W}$ . The lifetime measurements in  $^{178,180}\text{W}$  were part of the commissioning experiments of the revised Orange spectrometer and successfully demonstrate its capabilities.

From these lifetimes, the  $E2$  transition strengths, quadrupole moments  $Q_r$ , and quadrupole deformation parameters  $\beta$  have been calculated and the  $B_{4/2}$  ratios have been extracted. The newly determined  $B_{4/2}$  ratios for  $^{176}\text{W}$  and  $^{180}\text{W}$  as well as the new  $\beta$  values of the  $4^+$  and  $6^+$  states led to a more complete picture of the evolution of the quadrupole deformation for the tungsten isotopes in this region. The interpretation of the  $R_{4/2}$  values close to the SU(3) limit was confirmed by the  $B_{4/2}$  values and the evolution of the  $B(E2; I \rightarrow I - 2)$  values over the low-spin yrast states within  $^{178,180}\text{W}$ . However, a clear interpretation for  $^{176}\text{W}$  as well as the general description of the tungsten isotopic chain with special regard to the neutron-deficient side is more complicated and requires further effort. A remeasurement with modern methods of the lifetimes of  $^{172,174}\text{W}$  is recommended, due to the high uncertainties of the lifetimes of the  $2_1^+$  and  $4_1^+$  states in  $^{172}\text{W}$  and of the  $6_1^+$  state in  $^{174}\text{W}$ .

The measured values have been compared with calculations in the IBM-1 framework. The theoretical calculations in combination with the experimental  $B(E2; I \rightarrow I - 2)$  values and the theoretical and experimental quadrupole deformations of the  $2_1^+$  state support the previous interpretation of the tungsten isotopes around midshell as deformed prolate rotors.

## ACKNOWLEDGMENTS

The authors would like to thank the operator staff of the FN Tandem accelerator. This work was supported by the DFG under Grant No. JO 391 16-2. G.H. acknowledges support from the API-IDEX funding. A.E. and V.K. acknowledge the support by the BMBF under Grant No. 05P15PKFNA.

- 
- [1] G. D. Dracoulis, P. M. Walker, and F. G. Kondev, *Rep. Prog. Phys.* **79**, 076301 (2016).
- [2] D. A. Meyer, V. Wood, R. F. Casten, C. R. Fitzpatrick, G. Graw, D. Bucurescu, J. Jolie, P. von Brentano, R. Hertzenberger, H.-F. Wirth, N. Braun, T. Faestermann, S. Heinze, J. L. Jerke, R. Krücken, M. Mahgoub, O. Möller, D. Muecher, and C. Scholl, *Phys. Rev. C* **74**, 044309 (2006).
- [3] U. Götz, H. C. Pauli, K. Alder, and K. Junker, *Nucl. Phys. A* **192**, 1 (1972).
- [4] R.F. Casten and N. Zamfir, *J. Phys. G: Nucl. Part. Phys.* **22**, 1521 (1996).
- [5] P.-A. Söderström, P. Walker, J. Wu, H. Liu, P. Regan, H. Watanabe, P. Doornenbal, Z. Korkulu, P. Lee, L. Jiajian, G. Lorusso, S. Nishimura, V. Phong, T. Sumikama, F. Xu, A. Yagi, G. Zhang, D. Ahn, T. Alharbi, and Z. Xu, *PoS INPC2016*, 072 (2017).
- [6] F. Iachello, *Phys. Rev. Lett.* **87**, 052502 (2001).
- [7] H. Xin, Z. Li-Hua, W. Xiao-Guang, H. Chuang-Ye, Z. Yun, L. Li-Hua, S. Hui-Bin, and L. Guang-Sheng, *Chin. Phys. Lett.* **28**, 020201 (2011).
- [8] O. Möller, Ph.D. thesis, Universität zu Köln (2005).
- [9] C. Fransen, A. Dewald, G. Friessner, M. Hackstein, J. Jolie, O. Möller, T. Pissulla, W. Rother, and K. O. Zell, *AIP Conf. Proc.* **1377**, 311 (2011).
- [10] P. Cejnar, J. Jolie, and R. F. Casten, *Rev. Mod. Phys.* **82**, 2155 (2010).
- [11] Krishna Kumar, *Phys. Rev. Lett.* **28**, 249 (1972).
- [12] D. Cline, *Annu. Rev. Nucl. Part. Sci.* **36**, 683 (1986).
- [13] V. Werner, P. von Brentano, and R. V. Jolos, *Phys. Lett. B* **521**, 146 (2001).
- [14] D. J. Rowe, P. S. Turner, and G. Rosensteel, *Phys. Rev. Lett.* **93**, 232502 (2004).
- [15] M.S. Basunia, *Nucl. Data Sheets* **107**, 791 (2006).
- [16] E. Achterberg, O. A. Capurro, and V. Marti, *Nucl. Data Sheets* **110**, 1473 (2009).
- [17] E. A. McCutchan, *Nucl. Data Sheets* **126**, 151 (2015).
- [18] M. Rudigier, J.-M. Régis, J. Jolie, K. O. Zell, and C. Fransen, *Nucl. Phys. A* **847**, 89 (2010).
- [19] M. Rudigier, P. M. Walker, R. L. Canavan, Zs. Podolyak, P. H. Regan, P.-A. Söderström, M. Lebois, J. N. Wilson, N. Jovancevic, A. Blazhev, J. Benito, S. Bottoni, M. Brunet, N. Cieplicka-Orynczak, S. Courtin, D. T. Doherty, L. M. Fraile, K. Hadynska-Klek, M. Heine, Å. W. Iskra *et al.*, *Phys. Lett. B* **801**, 135140 (2020).
- [20] A. Dewald, S. Harissopulos, and P. von Brentano, *Z. Phys. A: At. Nucl.* **334**, 163 (1989).
- [21] K. S. Krane, *Introductory Nuclear Physics*, Vol. 465 (Wiley, New York, 1988).
- [22] J.-M. Régis, Th. Materna, S. Christen, C. Bernards, N. Braun, G. Breuer, Ch. Fransen, S. Heinze, J. Jolie, T. Meersschant, G. Pascovici, M. Rudigier, L. Steinert, S. Thiel, N. Warr, and K. O. Zell, *Nucl. Instrum. Methods Phys. Res., Sect. A* **606**, 466 (2009).
- [23] O. Kofoed-Hansen, J. Lindhard, and O. B. Nielsen, *Mat. Fys. Medd. K. Dan. Vidensk. Selsk.* **25**, 356 (1950).
- [24] M. Rudigier, K. Nomura, M. Dannhoff, R.-B. Gerst, J. Jolie, N. Saed-Samii, S. Stegemann, J.-M. Régis, L. M. Robledo, R. Rodríguez-Guzmán, A. Blazhev, Ch. Fransen, N. Warr, and K. O. Zell, *Phys. Rev. C* **91**, 044301 (2015).
- [25] A. Arima and F. Iachello, in *Advances in Nuclear Physics* (Springer, Boston, 1984), pp. 139–200.
- [26] J.-M. Régis, H. Mach, G. S. Simpson, J. Jolie, G. Pascovici, N. Saed-Samii, N. Warr, A. Bruce, J. Degenkolb, L. M. Fraile, C. Fransen, D. G. Ghita, S. Kisyov, U. Koester, A. Korgul, S. Lalkovski, N. Marginean, P. Mutti, B. Olaizola, Z. Podolyak *et al.*, *Nucl. Instrum. Methods Phys. Res., Sect. A* **726**, 191 (2013).
- [27] A. Dewald, O. Möller, and P. Petkov, *Prog. Part. Nucl. Phys.* **67**, 786 (2012).
- [28] J.-M. Régis, Th. Materna, G. Pascovici, S. Christen, A. Dewald, C. Fransen, J. Jolie, P. Petkov, and K. O. Zell, *Rev. Sci. Instrum.* **81**, 113505 (2010).
- [29] J.-M. Régis, Diplomarbeit, Universität zu Köln (2007).
- [30] M. de Huu, Diplomarbeit, Universität Fribourg, Schweiz (1998).
- [31] E. Moll, Diplomarbeit, Technische Hochschule München (1961).
- [32] G. Soff, J. Reinhardt, B. Müller, and W. Greiner, *Phys. Rev. Lett.* **43**, 1981 (1979).
- [33] J.-M. Régis, N. Saed-Samii, M. Rudigier, S. Ansari, M. Dannhoff, A. Esmaylzadeh, C. Fransen, R.-B. Gerst, J. Jolie, V. Karayonchev, C. Müller-Gatermann, and S. Stegemann, *Nucl. Instrum. Methods Phys. Res., Sect. A* **823**, 72 (2016).
- [34] *User's Manual Digital Gamma Finder (DGF) PIXIE-16* (XIA, LLC, Newark, CA, 2009).
- [35] L. G. Mann, J. B. Carlson, R. G. Lanier, G. L. Struble, W. M. Buckley, D. W. Heikkinen, I. D. Proctor, and R. K. Sheline, *Phys. Rev. C* **19**, 1191 (1979).
- [36] J. Burde, R. M. Diamond, and F. S. Stephens, *Nucl. Phys.* **85**, 481 (1966).
- [37] A. Linnemann, Ph.D. thesis, University of Cologne (2005).
- [38] L. Knafla, G. Häfner, J. Jolie, J.-M. Régis, V. Karayonchev, A. Blazhev, A. Esmaylzadeh, C. Fransen, A. Goldkuhle, S. Herb *et al.*, *Phys. Rev. C* **102**, 044310 (2020).
- [39] L. Kaya, A. Vogt, P. Reiter, M. Siciliano, N. Shimizu, Y. Utsuno, H.-K. Wang, A. Gargano, L. Coraggio, N. Itaco, K. Arnsward, D. Bazzacco, B. Birkenbach, A. Blazhev, A. Bracco, B. Bruyneel, L. Corradi, F. C. L. Crespi, G. de Angelis, M. Droste *et al.*, *Phys. Rev. C* **100**, 024323 (2019).
- [40] V. Karayonchev, J.-M. Régis, J. Jolie, A. Blazhev, R. Altenkirch, S. Ansari, M. Dannhoff, F. Diel, A. Esmaylzadeh, C. Fransen, R.-B. Gerst, K. Moschner, C. Müller-Gatermann,

- N. Saed-Samii, S. Stegemann, N. Warr, and K. O. Zell, *Phys. Rev. C* **95**, 034316 (2017).
- [41] A. Esmaylzadeh, L. M. Gerhard, V. Karayonchev, J.-M. Régis, J. Jolie, M. Bast, A. Blazhev, T. Braunroth, M. Dannhoff, F. Dunkel, C. Fransen, G. Häfner, L. Knafla, M. Ley, C. Müller-Gatermann, K. Schomacker, N. Warr, and K.-O. Zell, *Phys. Rev. C* **98**, 014313 (2018).
- [42] M. Wilhelm, J. Eberth, G. Pascovici, E. Radermacher, H. G. Thomas, P. von Brentano, H. Prade, and R. M. Lieder, *Nucl. Instrum. Methods Phys. Res., Sect. A* **381**, 462 (1996).
- [43] Z. Bay, *Phys. Rev.* **77**, 419 (1950).
- [44] J.-M. Régis, A. Esmaylzadeh, J. Jolie, V. Karayonchev, L. Knafla, U. Köster, Y. H. Kim, and E. Strub, *Nucl. Instrum. Methods Phys. Res., Sect. A* **955**, 163258 (2020).
- [45] L. Knafla, P. Alexa, U. Köster, G. Thiamova, J.-M. Régis, J. Jolie, A. Blanc, A. M. Bruce, A. Esmaylzadeh, L. M. Fraile, G. de France, G. Häfner, S. Ilieva, M. Jentschel, V. Karayonchev, W. Korten, T. Kröll, S. Lalkovski, S. Leoni, H. Mach *et al.*, *Phys. Rev. C* **102**, 054322 (2020).
- [46] A. Esmaylzadeh, J.-M. Régis, Y. H. Kim, U. Köster, J. Jolie, V. Karayonchev, L. Knafla, K. Nomura, L. M. Robledo, and R. Rodríguez-Guzmán, *Phys. Rev. C* **100**, 064309 (2019).
- [47] T. Kibédi, Jr., T. W. Burrows, M. B. Trzhaskovskaya, P. M. Davidson, and C. W. Nestor, Jr., *Nucl. Instrum. Methods Phys. Res., Sect. A* **589**, 202 (2008).
- [48] B. Saha, Ph.D. thesis, Universität zu Köln (2004).
- [49] R. F. Casten, *Nuclear Structure from a Simple Perspective*, Vol. 23 (Oxford University Press, Oxford, 2000).
- [50] B. Singh, *Nucl. Data Sheets* **75**, 199 (1995).
- [51] M. M. Minor, *Nucl. Data Sheets* **10**, 515 (1973).
- [52] B. Singh, *Nucl. Data Sheets* **130**, 21 (2015).
- [53] C. M. Baglin, *Nucl. Data Sheets* **111**, 275 (2010).
- [54] R. B. Firestone, *Nucl. Data Sheets* **55**, 583 (1988).
- [55] J. Wiederhold, V. Werner, R. Kern, N. Pietralla, D. Bucurescu, R. Carroll, N. Cooper, T. Daniel, D. Filipescu, N. Florea, R.-B. Gerst, D. Ghita, L. Gurgi, J. Jolie, R. S. Ilieva, R. Lica, N. Marginean, R. Marginean, C. Mihai, I. O. Mitu *et al.*, *Phys. Rev. C* **99**, 024316 (2019).
- [56] N. V. Zamfir, G. Hering, R. F. Casten, and P. Paul, *Phys. Lett. B* **357**, 515 (1995).
- [57] A. Bohr and B. R. Mottelson, *Nuclear Structure: Vol. 1* (World Scientific, Singapore, 1969).
- [58] M. A. El-Khosht, *Nuovo Cimento A* **106**, 875 (1993).
- [59] B. Cederwall, M. Doncel, Ö. Aktas, A. Ertoprak, R. Liotta, C. Qi, T. Grahm, D. M. Cullen, B. S. Nara Singh, D. Hodge, M. Giles, S. Stolze, H. Badran, T. Braunroth, T. Calverley, D. M. Cox, Y. D. Fang, P. T. Greenlees, J. Hilton, E. Ideguchi *et al.*, *Phys. Rev. Lett.* **121**, 022502 (2018).
- [60] R. M. Diamond and F. S. Stephens, *Annu. Rev. Nucl. Part. Sci.* **30**, 85 (1980).
- [61] K. Heyde, P. Van Isacker, J. Jolie, J. Moreau, and M. Waroquier, *Phys. Lett. B* **132**, 15 (1983).
- [62] K. Heyde, J. Jolie, P. Van Isacker, J. Moreau, and M. Waroquier, *Phys. Rev. C* **29**, 1428 (1984).
- [63] P. E. Garrett, M. Zielińska, and E. Clément, *Prog. Part. Nucl. Phys.* **124**, 103931 (2022).
- [64] J. Gascon, P. Taras, P. Van Esbroek, H. R. Andrews, D. C. Radford, D. Ward, and A. Christy, *Nucl. Phys. A* **472**, 558 (1987).
- [65] C. Y. Wu, D. Cline, E. G. Vogt, W. J. Kernan, T. Czosnyka, K. G. Helmer, R. W. Ibbotson, A. E. Kavka, B. Kotlinski, and R. M. Diamond, *Nucl. Phys. A* **533**, 359 (1991).
- [66] A. Arima and F. Iachello, *Phys. Rev. Lett.* **35**, 1069 (1975).
- [67] A. Arima and F. Iachello, *Annu. Rev. Nucl. Part. Sci.* **31**, 75 (1981).
- [68] D. D. Warner and R. F. Casten, *Phys. Rev. Lett.* **48**, 1385 (1982).
- [69] A. Arima and F. Iachello, *Ann. Phys.* **111**, 201 (1978).
- [70] A. Arima and F. Iachello, *Ann. Phys.* **281**, 2 (2000).
- [71] K. Nomura, T. Otsuka, N. Shimizu, and L. Guo, *Phys. Rev. C* **83**, 041302(R) (2011).
- [72] S. Heinze, Ph.D. thesis, Universität zu Köln (2008).
- [73] T. Kibedi, G. D. Dracoulis, A. P. Byrne, and P. M. Davidson, *Nucl. Phys. A* **688**, 669 (2001).
- [74] B. Saygi, D. T. Joss, R. D. Page, T. Grahm, J. Simpson, D. O'Donnell, G. Alharshan, K. Auranen, T. Bäck, S. Boening, T. Braunroth, R. J. Carroll, B. Cederwall, D. M. Cullen, A. Dewald, M. Doncel, L. Donosa, M. C. Drummond, F. Ertuğral, S. Ertürk *et al.*, *Phys. Rev. C* **96**, 021301 (2017).